


Cite this: *Nanoscale Adv.*, 2022, 4, 1779

# Efficient charge transfer from organometal lead halide perovskite nanocrystals to free base meso-tetraphenylporphyrins†

Abha Jha, Hari Shankar, Sandeep Kumar, Muniappan Sankar and Prasenjit Kar \*

The efficient charge transfer from methylammonium lead halide, MAPbX<sub>3</sub> (X = Br, I), perovskite nanocrystals (PNCs) to 5,10,15,20-tetraphenylporphyrin (TPP) molecules has been investigated in detail. The hydrophobically-capped MAPbX<sub>3</sub> PNCs exhibited bright fluorescence in the solution state. However, in the presence of TPP, the fluorescence intensity was quenched, which is ascribed to the electron transfer from the PNCs to TPP. Photoluminescence (PL) spectroscopy and absolute quantum yield measurements were used to evaluate the fluorescence quenching. This efficient fluorescence quenching leads to an increase in the quenching efficiency value. The quenching of fluorescence intensity is not attributed to the change in lifetime, as evidenced by time-correlated single-photon counting (TCSPC) measurements, suggesting a static electron transfer from the PNCs to TPP molecules. Such a static fluorescence quenching corresponds to the adsorption of TPP onto the surface of hydrophobic PNCs, and has been examined *via* transmission electron microscopy (TEM). Cyclic voltammetry (CV) studies were used to compare the PNCs and PNCs@TPP nanocomposites, revealing that the electron transfer process takes place from the PNCs to the organic acceptor TPP molecules.

Received 27th November 2021  
Accepted 18th February 2022

DOI: 10.1039/d1na00835h

rsc.li/nanoscale-advances

## Introduction

Organic-inorganic hybrid halide perovskites have been extensively developed<sup>1,2</sup> due to their many intriguing properties, including narrow emission bandwidth,<sup>3</sup> size-tunable optical properties,<sup>4,5</sup> cost effectiveness, excellent quantum yield,<sup>6</sup> and photostability.<sup>7</sup> The commendable properties of these materials are very important in several optoelectronic devices,<sup>8,9</sup> such as lasers,<sup>10–12</sup> light-emitting diodes,<sup>13,14</sup> solar cells,<sup>15,16</sup> photodetectors,<sup>17,18</sup> and sensors.<sup>19</sup> The large surface-to-volume ratio of perovskite nanocrystals (PNCs) leads to a high proportion of surface atoms with surface states and dangling bonds.<sup>20,21</sup> Besides their ease of preparation, hybrid lead halide perovskites have sparked a lot of research interest due to their technological relevance. Additionally, extended  $\pi$ -conjugation, a basic N4 core, and the rigid and planar structure of porphyrin molecules play a crucial role in improving device performance due to their distinct electronic and photochemical properties.<sup>22–24</sup> These molecules are utilized in charge generation, light harvesting, and biochemical processes.<sup>25</sup>

Due to the quantum confinement effect, PNCs show intense fluorescence,<sup>26,27</sup> which is regulated by chemical composition

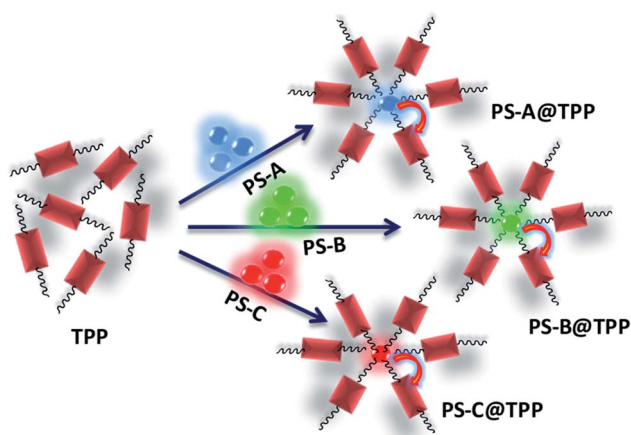
and bandgap engineering, and exhibit greater potential than perovskite films. Most hybrid halide perovskites are synthesized by the ligand-assisted reprecipitation (LARP) method using a capping ligand<sup>28</sup> or on the surface of substrate.<sup>29</sup> The tuning of the emission color of these perovskite nanocrystals from the visible to near-infrared (NIR) region is one of their fundamental advantages, which is achieved by the preparation of mixed halide perovskites through the post-synthesis halide exchange reaction and mixed halide precursors. This halide-dependent tunability of PL color results from the modification of band-edge states.<sup>30</sup>

Moreover, porphyrin-based systems have electron-transfer properties due to their exceptional photoelectric properties and broad absorption coefficient in the visible region.<sup>31,32</sup> The main reasons for selecting TPP as an electron acceptor over other electron accepting materials are its good solubility in common solvents, high mobility, appropriate energy-level alignment and strong light harvesting potential.<sup>33</sup> As a result, combining the properties of perovskite nanomaterials and porphyrins to create a nanocomposite will significantly improve their properties and result in further applications in optoelectronics. Currently, preparing perovskite-based nanocomposites with the electron-transfer phenomenon is one of the most prominent research areas. For example, Sundstrom *et al.*<sup>34</sup> pinpointed the electron transfer study of a hybrid metal halide perovskite with an organic acceptor molecule. Sargent *et al.*<sup>35</sup> reported the improved photocurrent response and stability of solar cells related to C<sub>60</sub>-layered perovskites, which corresponds to the

Department of Chemistry, Indian Institute of Technology Roorkee, Haridwar, Uttarakhand- 247667, India. E-mail: kar.prasen@gmail.com; prasenjit.kar@cy.iitr.ac.in

† Electronic supplementary information (ESI) available. See DOI: 10.1039/d1na00835h





**Scheme 1** Schematic representation of the electron transfer from  $\text{MAPbX}_3$  to TPP.

removal of grain boundaries and surface defect passivation in perovskites by  $\text{C}_{60}$ . Electron transport from perovskite to mesoporous titanium dioxide was studied by Gratzel *et al.*<sup>36</sup> An earlier study explored the transfer of electrons from donor PNCs to classical acceptors such as  $\text{TiO}_2$ ,<sup>37</sup> perylenes,<sup>38</sup> fullerenes,<sup>39,40</sup> benzoquinone,<sup>41</sup> and carbon nanotubes.<sup>42</sup> In this context, Tang *et al.*<sup>43</sup> used a diammonium porphyrin to study the charge transfer dynamics in  $\text{CsPbBr}_3$  nanocrystals. Recently, Patra *et al.*<sup>44</sup> demonstrated the charge transfer properties of  $\text{CsPbBr}_3$  PNCs with 5,10,15,20-tetrakis(4'-pyridyl)porphyrin.

In this work, we explicate the emission behavior of methylammonium lead halide ( $\text{MAPbX}_3$ ) PNCs in solutions with or without TPP. The  $\text{MAPbX}_3$  perovskite solution in the presence of TPP exhibits charge transfer and has been studied using photoluminescence (PL) spectroscopy, absolute photoluminescence quantum yield (PLQY) values and the time-correlated single-photon count (TCSPC) technique. Herein, TPP acts as an electron acceptor, and quenching of the emission of blue, green, and red luminescent PNCs has been recorded using PL spectra. A schematic representation of the electron transfer study is shown in Scheme 1. Meanwhile, the TCSPC measurement reveals the static fluorescence quenching of the PNCs. The details of the synthesis of the  $\text{MAPbBr}_3$  and  $\text{MAPbI}_3$  PNCs and TPP solutions are mentioned in the experimental section.

### Characterization

The UV-vis absorption spectra were recorded using a Shimadzu UV-1800 spectrophotometer in the range of 200 to 800 nm. A Horiba Scientific Fluoromax-4C spectrophotometer was used to monitor the photoluminescence and excitation spectra. To record the absolute quantum yield values of the nanocomposites, an Edinburgh FLS 980 instrument was used. A Rigaku-Smart Lab was used to record the X-ray diffraction (XRD) patterns by making a thin film with a Cu target and an angle range of  $10^\circ$  to  $50^\circ$ . TCSPC measurements were taken with a Horiba Jobin Yvon Fluorocube that was assembled with nano LEDs and spectral LEDs used as the excitation source. Fourier

transform infrared (FTIR) spectroscopy was carried out using a Thermo Scientific Nicolet 6700. X-ray photoelectron (XPS) spectroscopy of the material was performed on an XPS instrument with model no. PHI 5000 Versa Probe III for the analysis of the surface. Transmission electron microscopy (TEM) images were recorded on a FEI TECHNI G2 20 S-TWIN. Electrochemical measurements were recorded with a CH instrument (CHI-620E) under argon atmosphere along with a three-electrode assembly, where Ag/AgCl was used as a reference electrode, platinum (Pt) wire as a counter electrode and 2 mm platinum button as a working electrode.  $^1\text{H}$  NMR spectra were recorded on a 500 MHz NMR spectrometer using  $\text{CDCl}_3$  solvent.

## Experimental details

### Materials

Lead(II) bromide (99%, Aldrich), oleylamine (Aldrich), oleic acid (Aldrich), methylamine solution (33 wt% in absolute ethanol, Aldrich), chloroform (Rankem), *N,N*-dimethylformamide (Thomas Baker), and hydrobromic acid (48 wt% in water, SRL). All of the chemicals and solvents were acquired commercially and used as received.

### Methylammonium bromide (MABr) synthesis

In a 50 mL round-bottom (RB) flask, 6 mL  $\text{CH}_3\text{NH}_2$  was added with 6 mL ethanol. Then, at room temperature, 5 mL 57% aqueous solution of HBr was added dropwise, followed by continuous stirring. To remove all solvents, the resulting solution was kept in a rotary evaporator at  $60^\circ\text{C}$  for 1 h. To obtain the recrystallized product, the solution was washed multiple times with diethyl ether, dried and stored in a vacuum for further characterization.

### Methylammonium iodide (MAI) synthesis

In a 50 mL RB flask, 6 mL  $\text{CH}_3\text{NH}_2$  was mixed with 6 mL ethanol. Then, HI (5 mL 57% aqueous solution) was added dropwise while stirring continuously at room temperature. The obtained solution was placed in a rotary evaporator at  $60^\circ\text{C}$  for 1 h to remove all solvents. Then, to obtain the recrystallized product, the solution was washed several times with diethyl ether, dried and stored in a vacuum for further characterization.

### Synthesis of blue-luminescent $\text{CH}_3\text{NH}_3\text{PbBr}_3$ PNCs (PS-A)

0.0112 g  $\text{CH}_3\text{NH}_3\text{Br}$  (0.1 mmol) and 0.0367 g  $\text{PbBr}_2$  (0.1 mmol) were dissolved in 1 mL DMF, forming a 0.1 mM solution. Next, 100  $\mu\text{L}$  oleic acid and 200  $\mu\text{L}$  oleylamine were added, followed by continuous stirring. Afterwards, 100  $\mu\text{L}$  of this mixture was injected into 3 mL chloroform, which showed a blue color when observed under the UV chamber.

### Synthesis of green-luminescent $\text{CH}_3\text{NH}_3\text{PbBr}_3$ PNCs (PS-B)

0.0112 g  $\text{CH}_3\text{NH}_3\text{Br}$  (0.1 mmol) and 0.0367 g  $\text{PbBr}_2$  (0.1 mmol) were dissolved in 1 mL DMF, forming a 0.1 mM solution. Then, 200  $\mu\text{L}$  oleic acid and 38  $\mu\text{L}$  oleylamine were added, followed by stirring. Afterwards, 100  $\mu\text{L}$  of this mixture was injected into



3 mL chloroform, which was green when observed under the UV chamber.

### Synthesis of red-luminescent $\text{CH}_3\text{NH}_3\text{PbI}_3$ (PS-C)

0.0112 g  $\text{CH}_3\text{NH}_3\text{I}$  (0.1 mmol) and 0.0461 g  $\text{PbI}_2$  (0.1 mmol) were dissolved in 1 mL DMF, forming a 0.1 mM solution. Then, 100  $\mu\text{L}$  oleic acid and 200  $\mu\text{L}$  oleylamine were added, followed by continuous stirring. Afterwards, 100  $\mu\text{L}$  of this mixture was injected into 3 mL chloroform, showing a red color when observed under the UV chamber.

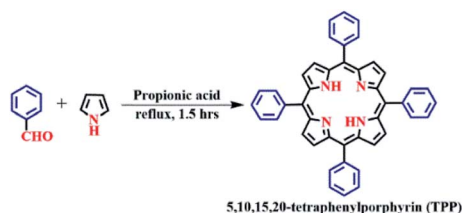
### Synthesis of TPP

TPP was synthesized using the Adler–Longo method (Scheme 2), as reported in the literature.<sup>45</sup> 4.41 mL benzaldehyde (43.24 mmol) and 3 mL pyrrole (43.24 mmol) were added to 180 mL hot propionic acid and refluxed for 90 min. The reaction mixture was cooled to room temperature and then filtered using a G4 sintered crucible. The purple crystalline solid was washed with methanol. The crude porphyrin was dissolved in a minimum amount of chloroform and purified by silica gel column chromatography using chloroform as the eluent, followed by recrystallization from a chloroform and methanol mixture (1 : 3, v/v). The purple crystalline product was dried under vacuum for 6 h. The yield was found to be 22% (1.5 g, 2.46 mmol), as shown in Scheme 2. The synthesized TPP was characterized by UV-vis and  $^1\text{H}$  NMR spectroscopy, mass spectrometry and elemental analysis. UV-vis ( $\text{CH}_2\text{Cl}_2$ ):  $\lambda_{\text{max}}$  (nm), ( $\log \epsilon$ ): 417 (5.58), 515 (4.19), 550 (3.83), 591 (3.68), and 647 (3.61).  $^1\text{H}$  NMR in  $\text{CDCl}_3$  (500 MHz,  $\delta$  in ppm): 8.85 (s, 8H,  $\beta$ -pyrrolic H), 8.22 (d, 8H, *meso*-*o*-phenyl H), 7.79–7.74 (d, 12H, *meso*-*m* & *p*-phenyl H), –2.76 (d, 2H, imino-H) (Fig. S1†).

### Synthesis of the $\text{CH}_3\text{NH}_3\text{PbX}_3@$ TPP nanocomposites

A stock solution of TPP was prepared by dissolving 0.08% w/v TPP in chloroform, following which, 50  $\mu\text{L}$  synthesized perovskite solution was injected into 2.5 mL chloroform used for emission quenching. The concentration of the PNC solution employed for characterization was  $0.66 \times 10^{-7}$  M, while the concentration of TPP molecules required to quench the fluorescence of the PNC solution was  $5 \times 10^{-7}$  M.

The UV-vis absorption spectra of green-luminescent (PS-B) and red-luminescent  $\text{MaPbI}_3$  perovskite nanocrystals (PS-C) with TPP were recorded at room temperature to track the optical properties of the  $\text{MaPbX}_3@$ TPP nanocomposites, as



Scheme 2 Synthesis of 5,10,15,20-tetraphenylporphyrin, TPP, using the Adler–Longo method.

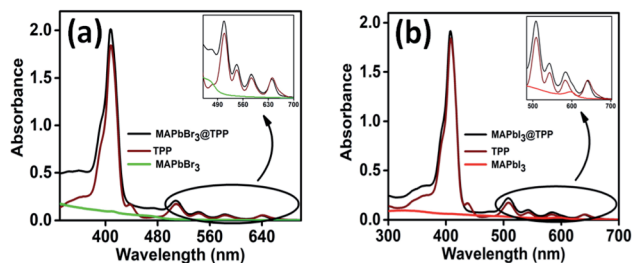


Fig. 1 Electronic absorption spectra of (a) PS-B and (b) PS-C PNCs in the presence of TPP in  $\text{CHCl}_3$  at 298 K.

shown in Fig. 1a and b. The absorption spectrum of TPP molecules dissolved in chloroform displays a characteristic Soret band (B band) at 417 nm, followed by four Q bands positions at 515, 550, 591, and 647 nm. The emission spectra of the  $\text{MAPbX}_3@$ TPP nanocomposites were also recorded in chloroform at room temperature, as shown in Fig. 2. We observe an almost 100% quenching of the fluorescence intensity of PS-A, PS-B and PS-C nanocrystals with TPP (Fig. 2a–c). This indicates that efficient electron transfer occurs from the PNCs to TPP. The fluorescence quenching was monitored with the successive addition of TPP solution from 20–140  $\mu\text{L}$ . An additional emission peak appeared at a higher wavelength in the range of 600–750 nm for the  $\text{MAPbX}_3@$ TPP nanocomposites, which corresponds to the characteristic emission peak of the porphyrin macrocycle.<sup>46</sup> This quenching of PL intensity is also indicated by the decrement in the quantum yield value of the nanocomposites, as mentioned in Table 1. This corroborated with the PL results, as shown in Fig. 2. Before the quenching experiment, we noticed a blue shift in the emission peak of the PNC samples as compared to a previous report<sup>47</sup> due to the dilution effect.

Furthermore, to examine the effect of solvent, we recorded the emission spectrum of the PNC solution in  $\text{CHCl}_3$  in the presence and absence of TPP, as illustrated in Fig. S2, ESI†, suggesting the trivial effect of the solvent in quenching the

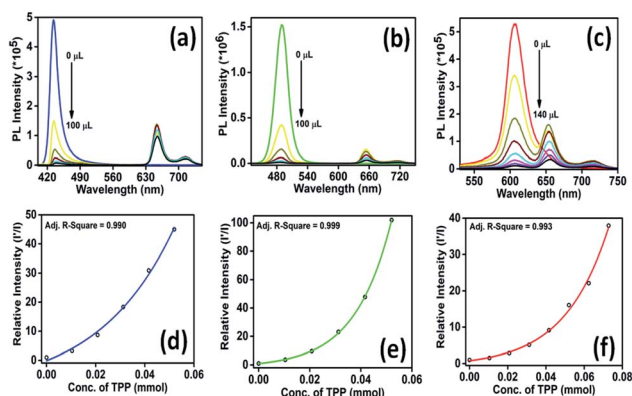


Fig. 2 PL quenching of (a) PS-A, (b) PS-B, and (c) PS-C PNC solutions supplemented with different concentrations of TPP. The relative intensity (PL) changes with different concentrations of TPP on the PL quenching of (d) PS-A, (e) PS-B, and (f) PS-C PNCs.



Table 1 Lifetime decay of the PNC solutions with TPP

	TPP volume	$A_1$	$A_2$	$A_3$	$\tau_1$	$\tau_2$	$\tau_3$	$\tau_{\text{avg}}$ (ns)	Quenching efficiency (%)	Quantum yield (%)
Blue-luminescent $\text{CH}_3\text{NH}_3\text{PbBr}_3$	0 $\mu\text{L}$	35.92	51.45	12.64	11.26	3.79	40.07	23.14	0	14
	20 $\mu\text{L}$	47.85	39.29	12.86	3.34	9.84	38.26	22.31	69.09	5
	100 $\mu\text{L}$	40.65	46.34	13.01	9.33	3.01	36.88	21.68	97.77	Less than 1
Green-luminescent $\text{CH}_3\text{NH}_3\text{PbBr}_3$	0 $\mu\text{L}$	74.22	25.78	—	6.65	20.09	—	13.53	0	27
	20 $\mu\text{L}$	73.14	26.86	—	6.47	19.31	—	13.18	72.55	6
	100 $\mu\text{L}$	71.98	28.02	—	6.38	19.03	—	13.17	99.01	Less than 1
Red-luminescent $\text{CH}_3\text{NH}_3\text{PbI}_3$	0 $\mu\text{L}$	34.09	55.98	9.93	6.52	12.55	44.71	22.00	0	62
	20 $\mu\text{L}$	33.82	57.50	8.67	6.35	12.74	45.40	21.30	35.40	25
	100 $\mu\text{L}$	35.65	55.71	8.64	6.40	12.85	41.15	19.45	93.78	13
	140 $\mu\text{L}$	38.20	53.59	8.22	6.61	12.95	40.65	18.93	98.63	8

fluorescence intensity of PNCs. This confirmed that the fluorescence quenching is caused by the adhesion of PNCs on TPP. The PL spectrum of the TPP solution displaying emission at 650 and 715 nm (at the same concentration used in the experiment) with  $\text{CHCl}_3$  is also observed and is shown in Fig. S3, ESI†. The self-excitation spectra of the PNCs, TPP as well as the PNCs@TPP nanocomposites are provided in Fig S4, ESI†. The nature of the quenching process can be understood by considering the Stern–Volmer plot. We obtained curves for the blue-, green- and red-luminescent perovskites instead of a linear line (Fig. 2d–f). The  $\text{MAPbX}_3$ @TPP nanocomposites probably show a non-linear Stern–Volmer plot due to static quenching or a combination of both static and dynamic quenching.<sup>48</sup>

Another way to distinguish whether the quenching is static, dynamic or a combination of both is to measure the lifetime of the luminescent PNC solution in the absence and presence of TPP used as a quencher.<sup>49</sup> The PL decay curves of the PNC solution without and with different concentrations of TPP (Fig. 3a–c) were determined by the time-correlated single-photon counting (TCSPC) technique. The fluorescence lifetimes (Table 1) of the samples remained unchanged regardless of the concentration of TPP. The constant fluorescence lifetime, along with a reduction in the number of emitted photons with an increasing amount of quencher, indicates that the excited state of the PNCs has been statically quenched by TPP.<sup>39a,40</sup> Meanwhile, the remaining fluorescence at a specific concentration of TPP indicates that the  $\text{MAPbX}_3$  PNCs have a trace of unadsorbed TPP. In other words, it can be assumed that the continuous reduction in the quantum efficiency of the nanocomposites without any significant change in lifetime indicates the adsorption of  $\text{MAPbX}_3$  PNCs onto the organic molecules.

The surface of the PNC solution is capped with oleic acid and oleylamine (hydrophobic ligands). The presence of these hydrophobic ligands causes the PNCs to adsorb on the surface of TPP molecules. The average lifetimes of the PNCs with TPP solution are provided in Table 1. The average lifetimes were evaluated using the formula:

$$\tau_{\text{avg}} = \frac{A_1\tau_1^2 + A_2\tau_2^2 + A_3\tau_3^2}{A_1\tau_1 + A_2\tau_2 + A_3\tau_3}$$

where  $\tau_{\text{avg}}$  is the average lifetime,  $A_1$ ,  $A_2$  and  $A_3$  are the pre-exponential factors, and the corresponding lifetimes are  $\tau_1$ ,  $\tau_2$  and  $\tau_3$ .

Quenching efficiency (QE) was calculated using the formula:

$$(\text{QE}) = \frac{I_0 - I}{I_0}$$

where  $I_0$  and  $I$  are the fluorescence intensities of the PNCs in the absence and presence of quencher, respectively.

The X-ray diffraction (XRD) patterns of the nanocomposites ( $\text{MAPbBr}_3$ @TPP) (Fig. S5, ESI†) have been recorded, showing the cubic phase of the perovskite nanocrystals. The XRD patterns of green-luminescent  $\text{MAPbBr}_3$  and red-luminescent  $\text{MAPbI}_3$  have also been analyzed (Fig. S6, ESI†), which confirm the phase of the PNCs, *i.e.* cubic and tetragonal, respectively.<sup>50</sup> The XRD patterns of PNCs@TPP and PNCs, as illustrated in Fig. S5, ESI, and S6, ESI†, show an additional peak at  $2\theta = 12.95^\circ$  related to unreacted  $\text{PbBr}_2$ . For PNCs@TPP, the XRD pattern is the same as that of the PNCs with no shift in the peak position, indicating that there is no phase distortion after binding with TPP.

To study the surface of the nanocomposites, X-ray photoelectron spectroscopy (XPS) analysis of the PS-B ( $\text{MAPbBr}_3$ ) PNCs with TPP was performed (Fig. 4). The survey scan of the nanocomposites revealed the presence of Br, Pb, C and N elements. To gain further insight into the elemental configuration, the high-resolution spectra of all the elements were recorded. The narrow scan shows Pb 4f peaks at 138.36 eV and 143.16 eV, corresponding to 4f 7/2 and 4f 5/2, respectively (Fig. 4b). The peaks at 68.41 eV and 69.52 eV are ascribed to Br 3d 5/2 and Br 3d 3/2, respectively. The peaks at 284.76 eV and 401.70 eV are associated with C 1s and N 1s, respectively (Fig. 4c and d). Furthermore, to confirm the mode of interaction

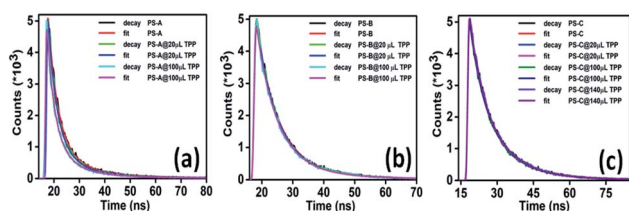


Fig. 3 PL decay curves of (a) PS-A (b) PS-B and (c) PS-C PNCs on the addition of TPP.



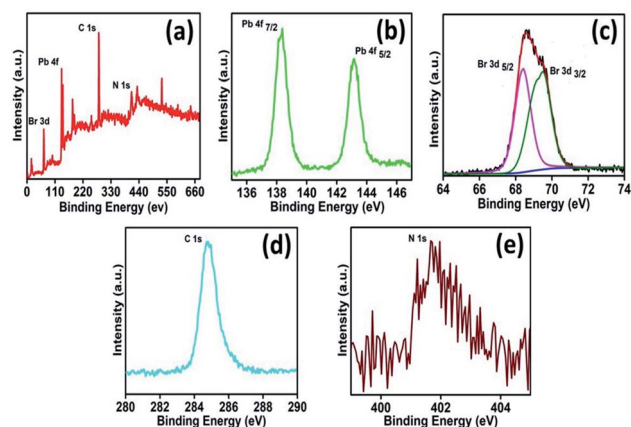


Fig. 4 XPS spectra of (a) survey scan, (b) lead, (c) deconvoluted bromide, (d) carbon and (e) nitrogen with TPP molecules.

between TPP and the PNCs,  $^1\text{H}$  nuclear magnetic resonance (NMR) (Fig. S7, ESI $^\dagger$ ) and infrared (IR) spectroscopic studies (Fig. S8, ESI $^\dagger$ ) of TPP in the presence and absence of the PNCs have been performed. The NMR spectra show that the protons of TPP molecules slightly shift in the presence of the PNCs, indicating a weak interaction with TPP (Fig. S7, ESI $^\dagger$ ). The FT-IR spectra also corroborate this observation; the stretching vibrational frequency of  $-\text{C}=\text{N}$  indicates that the pyrrole ring present at  $1638\text{ cm}^{-1}$  in TPP shifts by  $10\text{ cm}^{-1}$  in the presence of the PNCs (Fig. S8, ESI $^\dagger$ ).

TEM images were used to study the morphology of TPP, PNCs and PNCs@TPP. The TEM images of TPP with scale bars of 100 nm (Fig. 5a), 500 nm (Fig. 5b) and 1  $\mu\text{m}$  (Fig. 5c) show its sheet-like morphology. The tunability in the morphology of the perovskite nanocrystal solution (Fig. 5d–f) is evidenced by these TEM images. The TEM images of the PS-A (Fig. 5d), PS-B (Fig. 5e) and PS-C (Fig. 5f) perovskite solutions display

quantum dot, nanoplate and quantum dot morphologies, respectively. The particle sizes of the blue- (Fig. 5g, 4.31 nm), green- (Fig. 5h, 9.80 nm) and red-luminescent (Fig. 5i, 3.11 nm) perovskite nanoparticles are calculated from the histogram plot. The interaction of TPP on the surface of the hydrophobically-capped PNCs is confirmed by the TEM images, as shown in Fig. 5j–l. These interactions cause electron transfer from the donor perovskite to the acceptor TPP molecules.

To measure the electrochemical properties, *i.e.* the reduction potential ( $E_{\text{red}}$ ) and oxidation potential ( $E_{\text{ox}}$ ), of the PNCs and PNCs@TPP nanocomposites in solution form, cyclic voltammetry (CV) was performed at 298 K in  $\text{CH}_2\text{Cl}_2$  using 0.1 M TBAPF $_6$  as a supporting electrolyte (Fig. 6).

With the introduction of TPP solution to the perovskite nanocrystals, the reduction and oxidation potentials of the PNCs exhibited anodic and cathodic shifts as compared to the original PNCs, as shown in Fig. 6a. This indicates that TPP molecules have a significant effect on redox potential.

From the CV analysis (Fig. 6a), the bandgap values of the PNCs, PNCs@TPP and TPP solutions are calculated to be 2.47 eV, 2.20 eV and 2.27 eV, respectively. The highest occupied molecular orbital (HOMO) and lowest unoccupied molecular orbital (LUMO) are calculated as mentioned in previous reports. $^{51}$

For the PNCs, the energy levels are  $-2.57\text{ eV}$  LUMO and  $-5.04\text{ eV}$  HOMO. For the PNCs@TPP nanocomposites, the energy levels are lower, with  $-3.64\text{ eV}$  LUMO and  $-5.84\text{ eV}$  HOMO, and the HOMO ( $-5.44\text{ eV}$ ) and LUMO ( $-3.17\text{ eV}$ ) energy levels have also been calculated for TPP. The band alignment of the HOMO and LUMO energy levels of MAPbBr $_3$  as well as the HOMO and LUMO energy levels of TPP molecules indicate that TPP molecules withdraw electron density from the excited state of the PNC solution, and cause electron transfer from the PNCs to TPP molecules, as depicted in Fig. 6b.

Due to the spectral overlap integral and adsorption of TPP to the PNCs, fluorescence resonance energy transfer (FRET) from the PNCs to TPP was suspected to be the reason for the fluorescence quenching of the PNCs by TPP. However, the efficacy of energy transfer is highly dependent on two parameters: (i) the number of anchoring groups and (ii) the binding ability of

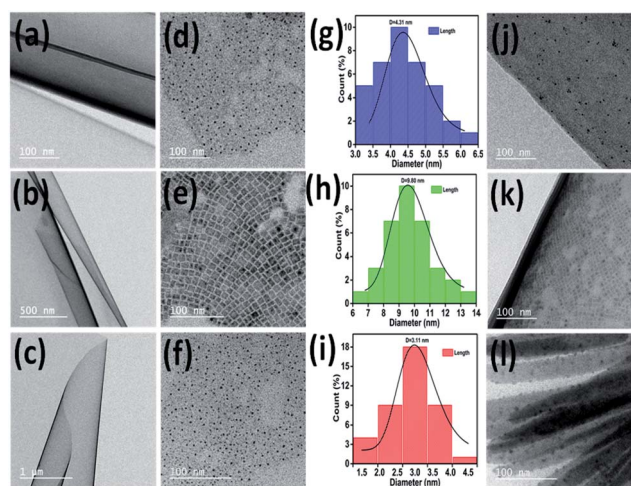


Fig. 5 TEM images of (a–c) TPP molecules at different scales. (d) PS-A, (e) PS-B and (f) PS-C with a scale bar of 100 nm. Particle size distribution of (g) PS-A, (h) PS-B and (i) PS-C. TEM images of (j) PS-A@TPP, (k) PS-B@TPP and (l) PS-C@TPP with a scale bar of 100 nm.

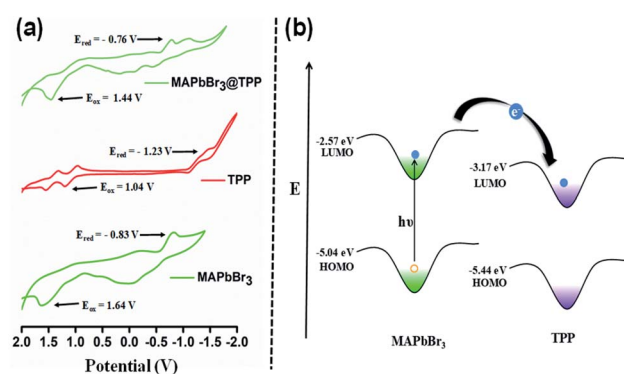


Fig. 6 (a) Comparative CVs (vs. Ag/AgCl) of MAPbBr $_3$ , TPP and MAPbBr $_3$ @TPP solutions. (b) Schematic representation of the energy-level alignment of MAPbBr $_3$  and TPP molecules.



acceptor molecules to the surface of the nanocrystals. However, TPP molecules have no valid anchor group. This leads to physical adsorption rather than anchoring of TPP molecules on the surface of the PNCs. Hence, the absence of the anchoring group and the lower emission intensity of porphyrin molecules as compared to other exciting fluorescent dyes excludes the possibility of FRET between the excited state of the PNCs and TPP.<sup>38,49</sup>

In conclusion, the charge transfer behaviour of MAPbX<sub>3</sub> perovskite nanocrystals as electron donors and the TPP macrocycle as the acceptor was demonstrated. The addition of TPP to the PNC solution causes fluorescence quenching with no change in fluorescence lifetime. The static fluorescence quenching of the perovskite solution is attributed to the adsorption of TPP onto the surface of hydrophobically-capped PNC nanocrystals, which was also analyzed by TEM. The mode of interaction of TPP with the PNCs has been analyzed by <sup>1</sup>H NMR and IR spectroscopy. Furthermore, by comparing the electrochemical properties of the PNCs@TPP nanocomposites with those of the PNCs, the LUMO as well as HOMO energy levels of the PNCs@TPP nanocomposites are significantly lower than those of the PNCs, indicating the effective transfer of electrons from the excited state of the PNCs to TPP molecules. These experimental findings not only open the way for understanding the electron transfer dynamics from MAPbBr<sub>3</sub> nanocrystals to TPP molecules but also offer the opportunity for utilizing porphyrin molecules as an alternative source of the electron transporting materials for next-generation technologies, especially in optoelectronics and related applications.

## Conflicts of interest

There is no conflict of interest to declare.

## Acknowledgements

The authors acknowledge the Institute Instrumentation Centre (IIC), IIT Roorkee, for the instrumentation facility. P. K. gratefully acknowledges the Science and Engineering Research Board (CRG/2020/000702), New Delhi, India, for their financial support. M. S. thanks the Science and Engineering Research Board (SER/CRG/2020/005958), New Delhi, for their financial support. A. J. acknowledges MHRD, India, for her doctoral fellowship. H. S. and S. K. acknowledge UGC, India, for their senior research fellowship.

## Notes and references

- M. D. Smith, B. A. Connor and H. I. Karunadasa, *Chem. Rev.*, 2019, **119**, 3104–3139.
- (a) L. Polavarapu, B. Nickel, J. Feldmann and A. S. Urban, *Adv. Energy Mater.*, 2017, **7**, 1700267; (b) A. Jha, P. Bansal, G. K. Nim and P. Kar, *Opt. Mater.*, 2021, **111**, 110660.
- W. Deng, H. Fang, X. Jin, X. Zhang and J. Jie, *J. Mater. Chem. C*, 2018, **6**, 4831–4841.
- H. Huang, L. Polavarapu, J. A. Sichert, A. S. Sussha, A. S. Urban and A. L. Rogach, *NPG Asia Mater.*, 2016, **8**, e328.
- L. Protesescu, S. Yakunin, M. I. Bodnarchuk, F. Krieg, R. Caputo, C. H. Hendon, R. X. Yang, A. Walsh and M. V. Kovalenko, *Nano Lett.*, 2015, **15**, 3692–3696.
- J.-H. Wei, X.-D. Wang, J.-F. Liao and D.-B. Kuang, *ACS Appl. Electron. Mater.*, 2020, **2**, 2707–2715.
- (a) Y. Wang, H. Zhang, T. Zhang, W. Shi, M. Kan, J. Chen and Y. Zhao, *Sol. RRL*, 2019, **3**, 1900197; (b) H. Shankar, A. Jha and P. Kar, *Mater. Adv.*, 2022, **3**, 658–664.
- S. D. Stranks and H. J. Snaith, *Nat. Nanotechnol.*, 2015, **10**, 391–402.
- S. T. Ha, R. Su, J. Xing, Q. Zhang and Q. H. Xiong, *Chem. Sci.*, 2017, **8**, 2522–2536.
- Y. Fu, H. Zhu, A. W. Schrader, D. Liang, Q. Ding, P. Joshi, L. Hwang, X.-Y. Zhu and S. Jin, *Nano Lett.*, 2016, **16**, 1000–1008.
- G. Xing, N. Mathews, S. S. Lim, N. Yantara, X. Liu, D. Sabba, M. Gratzel, S. Mhaisalkar and T. C. Sum, *Nat. Mater.*, 2014, **13**, 476–480.
- S. A. Veldhuis, P. P. Boix, N. Yantara, M. Li, T. C. Sum, N. Mathews and S. G. Mhaisalkar, *Adv. Mater.*, 2016, **28**, 6804–6834.
- N. Wang, L. Cheng, R. Ge, S. Zhang, Y. Miao, W. Zou and W. Huang, *Nat. Photonics*, 2016, **10**(11), 699–704.
- S. D. Stranks and H. J. Snaith, *Nat. Nanotechnol.*, 2015, **10**(5), 391–402.
- M. T. Hörantner, T. Leijtens, M. E. Ziffer, G. E. Eperon, M. G. Christoforo, M. D. McGehee and H. J. Snaith, *ACS Energy Lett.*, 2017, **2**(10), 2506–2513.
- Q. Lin, A. Armin, R. C. R. Nagiri, P. L. Burn and P. Meredith, *Nat. Photonics*, 2015, **9**(2), 106–112.
- (a) P. Bansal and P. Kar, *Chem. Commun.*, 2019, **55**, 6543–6546; (b) M. V. kovalenko, L. Protesescu and M. I. Bodnarchuk, *Science*, 2017, **358**, 745–750.
- Y. Wang, Z. Lv, Q. Liao, H. Shan, J. Chen, Y. Zhou, L. Zhou, X. Chen, V. A. Roy and Z. Wang, *Adv. Mater.*, 2018, **30**, 1800327.
- M.-A. Stoeckel, M. Gobbi, S. Bonacchi, F. Liscio, L. Ferlauto, E. Orgiu and P. Samorì, *Adv. Mater.*, 2017, **29**, 1702469.
- D. A. Wheeler and J. Z. Zhang, *Adv. Mater.*, 2013, **25**, 2878–2896.
- B. Luo, Y. C. Pu, S. A. Lindley, Y. Yang, L. Lu, Y. Li, X. Li and J. Z. Zhang, *Angew. Chem., Int. Ed.*, 2016, **55**, 8864–8868.
- T. Higashino, Y. Fujimori, I. Nishimura and H. Imahori, *J. Porphyrins Phthalocyanines*, 2020, **24**, 67–74.
- K. Kurlekar, A. Anjali, S. Sonalin, P. M. Imran and S. Nagarajan, *ACS Appl. Electron. Mater.*, 2020, **2**(10), 3402–3408.
- W. Li, Z. Liu, H. Wu, Y.-B. Cheng, Z. Zhao and H. He, *J. Phys. Chem. C*, 2015, **119**(10), 5265–5273.
- F. Li, S. I. Yang, Y. Ciringh, J. Seth, C. H. Martin, D. L. Singh, D. Kim, R. R. Birge, D. F. Bocian, D. Holten and J. S. Lindsey, *J. Am. Chem. Soc.*, 1998, **120**, 10001–10017.
- Q. A. Akkerman, S. G. Motti, A. R. Srimath Kandada, E. Mosconi, V. D'Innocenzo, G. Bertoni, S. Marras, B. A. Kamino, L. Miranda, F. de Angelis, A. Petrozza, M. Prato and L. Manna, *J. Am. Chem. Soc.*, 2016, **138**, 1010–1016.



- 27 G. C. Adhikari, H. Zhu, P. A. Vargas and P. Zhu, *J. Phys. Chem. C*, 2018, **122**(26), 15041–15046.
- 28 A. Jha, H. Shankar and P. Kar, *New J. Chem.*, 2022, **46**, 844–850.
- 29 A. Kojima, M. Ikegami, K. Teshima and T. Miyasaka, *Chem. Lett.*, 2012, **41**, 397–399.
- 30 L. Chouhan, S. Ghimire, C. Subrahmanyam, T. Miyasaka and V. Biju, *Chem. Soc. Rev.*, 2020, **49**, 2869–2885.
- 31 K. Zeng, Z. Tong, L. Ma, W.-H. Zhu, W. Wua and Y. Xie, *Energy Environ. Sci.*, 2020, **13**, 1617–1657.
- 32 J. Yang, J. Jing and Y. Zhu, *Adv. Mater.*, 2021, **33**, 2101026.
- 33 X. Yin, Z. Song, Z. Li and W. Tang, *Energy Environ. Sci.*, 2020, **13**, 4057–4086.
- 34 C. S. Ponseca Jr, E. M. Hutter, P. Piatkowski, B. Cohen, T. Pascher, A. Douhal, A. Yartsev, V. Sundström and T. J. Savenije, *J. Am. Chem. Soc.*, 2015, **137**, 16043–16048.
- 35 J. Xu, A. Buin, A. H. Ip, W. Li, O. Voznyy, R. Comin, M. Yuan, S. Jeon, Z. Ning, J. J. McDowell, P. Kanjanaboos, J.-P. Sun, X. Lan, L. N. Quan, D. H. Kim, I. G. Hill, P. Maksymovych and E. H. Sargent, *Nat. Commun.*, 2015, **6**, 7081.
- 36 A. Marchioro, J. Teuscher, D. Friedrich, M. Kunst, R. Krol, T. Moehl, M. Gratzel and J.-E. Moser, *Nature*, 2014, **508**, 250–255.
- 37 R. A. Scheidt, E. Kerns, P. V. Kamat and J. Phys, *Chem. Lett.*, 2018, **9**(20), 5962–5969.
- 38 R. Zhu, C. Gao, T. Sun, L. Shen, D. Sun and X. Li, *Langmuir*, 2016, **32**, 3294–3299.
- 39 (a) V. C. Nair, C. Muthu, A. L. Rogach, R. Kohara and V. Biju, *Angew. Chem., Int. Ed.*, 2017, **56**, 1214–1218; (b) S. Ghimire, V. C. Nair, C. Muthu, K. Yuyama, M. Vacha and V. Biju, *Nanoscale*, 2019, **11**, 9335–9340.
- 40 B. M. Sachith, T. Okamoto, S. Ghimire, T. Umeyama, Y. Takano, H. Imahori and V. Biju, *J. Phys. Chem. Lett.*, 2021, **12**, 8644–8651.
- 41 K. Wu, G. Liang, Q. Shang, Y. Ren, D. Kong and T. Lian, *J. Am. Chem. Soc.*, 2015, **137**, 12792–12795.
- 42 P. Bansal, X. Zhang, H. Wang, P. Kar and W. W. Yu, *Nanoscale Adv.*, 2020, **2**, 808–813.
- 43 X. X. Feng, X. D. Lv, Q. Liang, J. Cao and Y. Tang, *ACS Appl. Mater. Interfaces*, 2020, **12**(14), 16236–16242.
- 44 G. Ghosh, K. Marjit, S. Ghosh, A. Ghosh, R. Ahammed, A. De Sarkar and A. Patra, *J. Phys. Chem. C*, 2021, **125**, 5859–5869.
- 45 (a) S. Kumar, N. Chaudhri, W. R. Osterloh, K. M. Kadish and M. Sankar, *Dalton Trans.*, 2021, **50**, 17086–17100; (b) W. R. Osterloh, S. Kumar, N. Chaudhri, Y. Fang, M. Sankar and K. M. Kadish, *Inorg. Chem.*, 2020, **59**, 16737–16746; (c) S. Shanmugathan, C. Edwards and R. W. Boyle, *Advances in modern synthetic Porphyrin Chemistry, Tetrahedron*, 2020, **56**, 1025–1146.
- 46 S. M. Rojas-Montoya, M. Vonlanthen, P. Porcu, G. Flores-Rojas, A. Ruiu, D. Morales-Morales and E. Rivera, *Dalton Trans.*, 2019, **48**, 10435–10447.
- 47 H. S. Yang, S. H. Noh, E. H. Suh, J. Jung, J. G. Oh, K. H. Lee and J. Jang, *ACS Appl. Mater. Interfaces*, 2021, **13**, 4374–4384.
- 48 A. Pal, S. Srivastava, P. Saini, S. Raina, P. P. Ingole, R. Gupta and S. Sapra, *J. Phys. Chem. C*, 2015, **119**(39), 22690–22699.
- 49 C. Muthu, A. Vijayan and V. C. Nair, *Chem. - Asian J.*, 2017, **12**(9), 988–995.
- 50 I. Levchuk, P. Herre, M. Brandl, A. Osvet, R. Hock, W. Peukert, P. Schweizer, E. Spiecker, M. Batentschuk and C. J. Brabec, *Chem. Commun.*, 2017, **53**, 244–247.
- 51 L. Pan, B. Hu, X. Zhu, X. Chen, J. Shang, H. Tan, W. Xue, Y. Zhu, G. Liu and R. W. Li, *J. Mater. Chem. C*, 2013, **1**, 4556–4564.

